ARTICLE

Check for updates

Stable Southern Hemisphere westerly winds throughout the Holocene until intensification in the last two millennia

Willem G. M. van der Bilt [1✉], William J. D'Andrea[2], Lea T. Oppedal[1], Jostein Bakke [1], Anne E. Bjune [3] & Maaike Zwier [3]

The Southern Hemisphere westerly winds sustain the Southern Ocean's role as one of Earth's main carbon sinks, and have helped sequester nearly half the anthropogenic CO_2 stored in the ocean. Observations show shifts in the vigor of this climate regulator, but models disagree how future change impacts carbon storage due to scarce baseline data. Here, we use the hydrogen isotope ratios of sedimentary lipids to resolve Holocene changes in Southern Hemisphere westerly wind strength. Our reconstruction reveals stable values until ~2150 years ago when aquatic compounds became more ^2H-enriched. We attribute this isotope excursion to wind-driven lake water evaporation, and regional paleoclimate evidence shows it marks a trend towards a negative Southern Annular Mode – the Southern Ocean's main mode of atmospheric variability. Because this shift is unmatched in the past 7000 years, our findings suggest that previously published millennium-long Southern Annular Mode indices used to benchmark future change may not capture the full range of natural variability.

[1] Department of Earth Science and Bjerknes Centre for Climate Research, University of Bergen, Bergen, Norway. [2] Lamont-Doherty Earth Observatory, Columbia University, New York, NY, USA. [3] Department of Biological Sciences and Bjerknes Centre for Climate Research, University of Bergen, Bergen, Norway. ✉email: willemvanderbilt@uib.no

The Southern Ocean covers 20% of the Earth's surface and has stored more than 40% of all anthropogenic carbon emissions sequestered by the oceans since the industrial revolution[1], while absorbing around 75% of the excess heat generated during this period[2]. This outsized role as a global climate regulator is attributed to the Southern Hemisphere westerly winds (SHW), which draw up deep water and mix it while encircling the Antarctic[3]. The vigor of the Southern Ocean's role as a carbon pump is modulated by the opposing effects of CO_2 uptake and outgassing at the sea surface[4]. This balance is strongly influenced by variations in the strength and position of the SHW[5]. These, in turn, are largely driven by the Southern annular mode (SAM)[6]: the main pattern of atmospheric climate variability over the Southern Ocean, which is typically described as the pressure difference between mid and high austral latitudes[7]. The SHW belt shifts poleward in the positive SAM polarity and expands equatorward during a negative SAM phasing[8].

Instrumental data reveal an increasingly positive SAM phasing and associated poleward SHW shift over the past decades[8,9], which has already intensified regional hydroclimate extremes[10]. While this recent (last ~50 years) trend is primarily attributed to a combination of anthropogenic ozone depletion and greenhouse gas emissions[11], recent studies indicate that natural SAM variability is substantial and cannot be explained by direct radiative forcing mechanisms alone[12,13]. These findings have drawn further attention to observational evidence for SAM modulation by other internal modes of climate change, most notably the El Niño-Southern Oscillation (ENSO)[14,15]. However, while such teleconnections can modify the impact of anthropogenic forcing on coupled SHW-SAM change[16], their dynamics remain poorly documented and incompletely understood[17]. This knowledge gap mainly stems from the scarcity and brevity of baseline data[8]: our knowledge of past SAM variability does not extend beyond the last millennium, and only two records span that entire period[12,13]. Longer paleoclimate timeseries are imperative to resolve the full range of natural variability and better represent future SHW-SAM behavior and its impact on atmospheric CO_2 concentrations[5,18].

Here, we present a record of centennial-scale variations in SHW strength over the past 7 ka based on lake sediments. To do so, we investigated a lacustrine sediment sequence from South Georgia (54.4°S and 36.6°W), a sub-Antarctic Island in the SHW core belt (Fig. 1a). To avoid the uncertainties (for example, lags or non-linearity) of wind-attributed feedbacks like changes in precipitation or temperature and their impact on vegetation[19], we rely on a less indirect measure of wind strength: sedimentary leaf wax hydrogen isotope ratios (δ^2H). Modern observations help constrain the climatic controls on the δ^2H values of source water used by plants in South Georgia. Compound-specific analysis reveals that the isotopic composition of lake water (recorded by aquatic plants) became ^2H-enriched compared to its meteoric source water (recorded by terrestrial plants). The direction and magnitude of this isotopic offset is indicative of evaporative water loss[20], a process that is typically wind-driven in similar closed (endorheic) basins in the SHW core belt[21].

Setting and approach

South Georgia (54.4°S and 36.6°W) is one of the few landmasses that is located year-round in the SHW core belt and, therefore, well-situated to detect the fingerprints of past variations in this globally relevant circulation system (see introduction). As can be seen in Fig. 1a, this belt contracts in summer and expands during winter. On longer timescales, SAM variations can cause similar latitudinal SHW shifts in response to changes in the meridional pressure gradient between 45°S and 60°S[7]. While we should note

that the relation between SAM and regional climate depends on the choice of index and data due to a lack of observations[22], the station-based Marshall SAM index reveals a negative correlation with re-analyzed wind stress on South Georgia for the period prior to 1979[23]—when SAM variability is attributed to natural variations captured by proxy records like ours[24]. Numerous studies have also linked SAM-related shifts in temperature and hydroclimate to island-wide changes in glacier extent or ecosystem dynamics[25–32]. Local weather observations from Grytviken (Fig. 1a) reveal a maritime subpolar climate with an average annual temperature of 2 °C and 1450 mm of evenly distributed yearly precipitation[23] (Fig. 1c).

Our study site—informally named Lake Diamond[29]—is located in the north-central part of South Georgia, in the Olsen Valley that abuts the Cumberland West Bay (Fig. 1b). The basin covers an area of ~0.1 km², sits at ~15 m a.s.l and has a maximum depth of 3.5 m. Vegetation is restricted to areas below 100 m a.s.l (Fig. 1b) and is dominated by tussock grass (*Festuca contracta*) and greater burnet (*Acaena magellanica*). Based on reconstructed glacigenic sediment fluxes, previous studies showed that meltwater from the up-valley Diamond glacier incidentally spilled into the lake during flood events over the past 7 ka[29,32]. Timeseries analysis of Sentinel-2 satellite imagery reveals that this has not happened since image acquisition commenced in 2015[33]. In the absence of in- or outlets, we consider the basin closed (endorheic): water is thus primarily sourced from precipitation falling in the ~1 km² Lake Diamond catchment (Fig. 1b). Satellite imagery also shows that our study site is typically snow- and ice-covered for 6 months and that ice-off occurs between late October and early November.

We present lipid biomarker analyzes from Lake Diamond sediments that were previously studied by[29]. The investigated sequences consist of 46 cm long surface core LDS2 and 246 cm piston core LDP2: based on a robust published radiocarbon chronology ($n = 24$), this record covers the past 10 ka. We restricted our analyses to the past 7.2 ka, when the Diamond basin was occupied by a lake. This interval is contained in the uppermost 221.5 cm of the composite record and has previously been described as units D and F by ref. [29].

To reconstruct sub-Antarctic surface climate change during this period, and assess its links to SHW core belt shifts, hydrogen isotope ratios (δ^2H) were measured on plant leaf wax samples ($n = 56$) from Lake Diamond sediments (see methods). For this purpose, we extracted, separated, quantified, and analyzed n-alkanes: aliphatic hydrocarbons produced by plants and preserved in sedimentary archives around the world[34]. δ^2H values of these lipid biomarkers track the δ^2H values of the source water used during biosynthesis[35–37].

Isotope values of precipitation are influenced by a range of parameters, including condensation temperature, evaporation, precipitation amount, and the source and pathway of moisture[38]: near South Georgia, all of these variables co-vary with SHW change[12,39–41]. Weather station data from nearby Grytviken (~10 km away) and interpolated precipitation isotopes reveal a strong positive ($R^2 = 0.92$, $p < 0$) relationship between modern (1905–2019 CE) surface temperatures and meteoric δ^2H (Figs. 1c, 2b)[23,42]. Based on observations and ice core data from James Ross Island (Fig. 1a)[43,44], this relationship could have existed throughout the past 7 ka. The isotope composition ($\mu = -60.3‰$, $2\sigma = 1.1‰$) of two modern samples furthermore indicates that lake water δ^2H values approximate the weighted local annual precipitation mean ($-67.5‰$), despite collection during the austral summer (February 2015). Figure 2a shows that evaporative loss of lighter ^{16}O and ^1H has a minor impact on modern lake water composition as our water samples plot just below the Local Meteoric Water Line (LMWL), constructed with data from
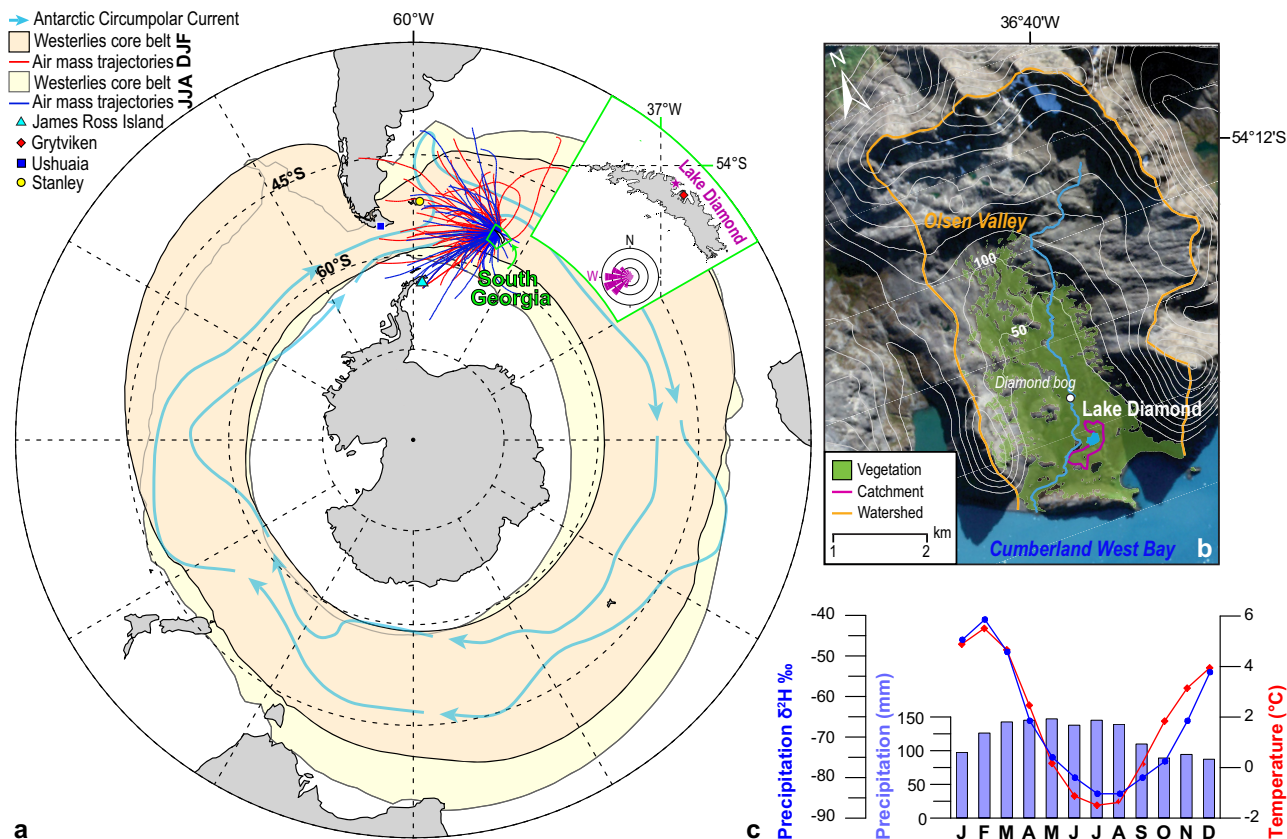
Fig. 1 Key localities and observations. a Overview map of the Southern Ocean with an inset of South Georgia, highlighting Lake Diamond as well as the nearest weather stations of Grytviken, Ushuaia, and Stanley in color coding that corresponds with Fig. 2. The average position and extent of the Southern Westerlies core belt, defined as areas where mean zonal wind speeds exceed 5 m/s⁻¹ between 1981–2010 CE[122], is shown for the Austral summer (DJF) and winter (JJA). The purple wind rose shows the prevalence of this dominant wind system. Forty-eight hours daily backward air mass trajectories from 2019 are shown for summer (red) and winter (blue)[123]. The long-term position of the Antarctic Circumpolar Current (ACC) is delimited in cyan by the Antarctic convergence to the South and the Sub-Antarctic front to the North after[124]. **b** Close-up of the Lake Diamond catchment and the wider Olsen valley as modified after[29]. Vegetated areas, defined as surfaces with normalized difference vegetation index (NDVI) values >0.3 during the growing season (January 2020)[33], are highlighted in green. Sentinel-2 satellite image courtesy of the ESA Copernicus Open Access Hub. **c** Long-term monthly local climatology based on 1905-2012 CE station data from nearby Grytviken[23] and spatial δ2H interpolation[42].

the nearest GNIP stations at Ushuaia (~2000 km away) and Stanley (~1500 km away)[45](Fig. 1a).

Results and discussion

Holocene lipid δ2H records lake water evaporation. Because modern meteoric δ2H correlates with seasonal temperature change in South Georgia, and Lake Diamond water δ2H integrates a somewhat enriched annual precipitation average (see Figs. 1c, 2), we expect reconstructed values to capture changes in temperature and evaporative 2H-enrichment. To better constrain this paleo signal, we disentangle the different plant sources producing our sedimentary *n*-alkanes and the environmental signals they record in the text below.

While aquatic photoautotrophs directly use lake water for biosynthesis[35], terrestrial plants use soil moisture[35], which is often isotopically skewed towards the growing season when biosynthesis occurs[46] and differently impacted by evaporative enrichment than lake water[47,48]. This is particularly true for closed (endorheic) basins like Lake Diamond due to their long water residence time[20]. To constrain these different δ2H source signatures, we differentiate between aquatic and terrestrial *n*-alkane producers. It has previously been argued that mid-chain (C$_{21}$-C$_{25}$) *n*-alkane homologs are produced by aquatic plants, whereas long-chain (C$_{27}$-C$_{33}$) compounds typically derive from

terrestrial vegetation[49,50]. Recent studies have called this generalization into question[51–53]. Here, we rely on reported *n*-alkane distributions from representative terrestrial vegetation at nearby Grytviken to understand the sources of *n*-alkanes in Lake Diamond (Fig. 1a)[54]. Critically, this selection comprises two species that dominate the Lake Diamond catchment today: tussock grass and greater burnet (see Fig. 3a). As can be seen in Fig. 4, mid-chain homologs are negligible in these terrestrial plants but abundant in sediment samples. This is in line with evidence from upwind southern Patagonia, where these compounds are attributed to aquatic macrophytes[55]. We thus argue that mid-chain *n*-alkanes are primarily synthesized by aquatic producers in Lake Diamond. In this respect, we note that moss patches in the catchment only contain traces of *Sphagnum*[32]—the only peat-forming species synthesizing considerable amounts of mid-chain *n*-alkanes[56,57]. The inference that mid- and long-chain homologs derive from different sources is supported by Principal Component Analysis (PCA: see methods). The ordination diagram of Fig. 5c separates these homologous groups on PC2. Based on these lines of reasoning, we infer that mid- and long-chain *n*-alkanes derive from aquatic and terrestrial plants, respectively.

Down-core *n*-alkane δ2H values can also be affected by vegetation shifts because of species-specific differences in apparent fractionation between source water and leaf
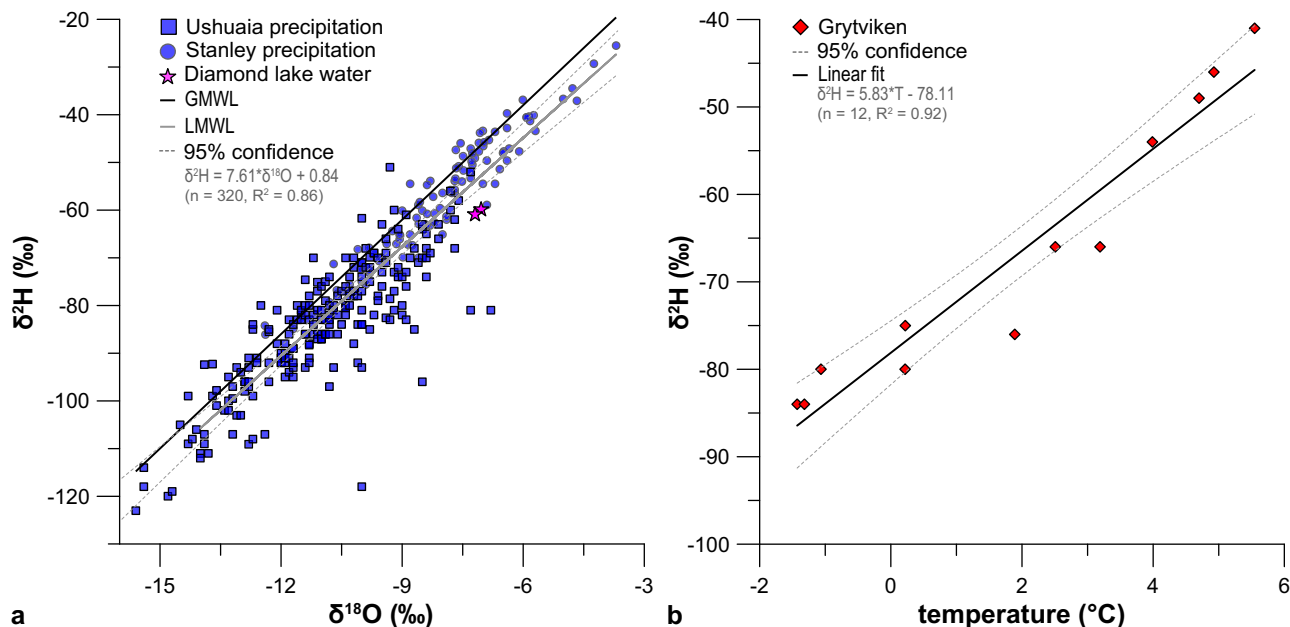
Fig. 2 Isotope characteristics of meteoric and lake water. a Relationships between source water precipitation hydrogen isotope values (δ^2H) and oxygen isotopes ($\delta^{18}O$) in samples collected between 1965–2016 CE from the most proximal weather stations in Stanley and Ushuaia along the global (GMWL: black) and local (LMWL: gray) waterlines[45]. **b** Monthly temperatures at the nearby (~10 km away) Grytviken weather station (see Fig. 1a)[23,42]. Regression fits with summary statistics between plotted variables are shown in gray. The pinks star ($n = 2$) in panel **a** highlights the isotope value of Lake Diamond water samples taken in February 2015.

waxes[35,58,59]. To constrain vegetation changes in the catchment area over the past 7 ka, we use palynological evidence and *n*-alkane Average Chain Length (ACL: see methods). The pollen data seen in Fig. 3a show that tussock grasses (*Festuca contracta*) and greater brunet (*Acaena magellanica*) have dominated terrestrial plant cover around Lake Diamond over the past 7 ka. The stable abundance of *Callitriche antarctica* and *Montia fontana*, the only mid-chain *n*-alkane-synthesizing macrophytes preserved in the Diamond pollen record, suggest aquatic vegetation also changed little[60]. Supporting this evidence, both ACL values and concentrations of mid-chain (C_{21}-C_{25}) and long-chain (C_{27}-C_{33}) homologs fluctuate around a stable mean throughout our study period (Fig. 3a–c). Finally, we find no relationship between *n*-alkane abundance and δ^2H values of various homologs, indicating that the inferred minor vegetation changes do not explain changes in isotope values (Fig. 5a, b).

Hydrogen isotope values of all analyzed *n*-alkanes are relatively stable on centennial timescales from the beginning of the Lake Diamond record until ~2150 cal. yr. BP (Fig. 6). Variability then visibly deviates from this long-term mean, as also indicated by change-point analysis (see methods). Deviation from the long-term mean is primarily captured by hydrogen isotope values of mid-chain aquatic homologs (δ^2H_{aq}), which become progressively more positive. In contrast, hydrogen isotope values of long-chain terrestrially derived homologs (δ^2H_{terr}) exhibit a different and more subdued response that does not significantly deviate from the long-term mean (Fig. 6b). As noted, modern water samples from Lake Diamond are indistinguishable from amount-weighted annual precipitation δ^2H values, which in turn track surface temperatures on South Georgia at seasonal timescales (Fig. 1c). Based on the calculated δ^2H-temperature dependence of 5.83‰ °C^{-1} (Fig. 2b), the observed ~100‰ δ^2H_{aq} shift to more positive values during the past two millennia would require ~17 degrees of warming. As local and regional temperature reconstructions reveal a shift towards moderately cooler annual (~1 °C) and growing season (~2 °C) conditions during this period

(Fig. 6a)[27,44,61], this is highly implausible. Furthermore, the dissimilarity between changes in δ^2H_{aq} and δ^2H_{terr} values suggests that at least one of these records does not simply reflect δ^2H values of precipitation. We also exclude large variations in precipitation seasonality: as the isotopic composition of soil moisture used by land plants is typically skewed towards the growing season when biosynthesis occurs[62], the observed isotopic enrichment of δ^2H_{aq} would also be captured by δ^2H_{terr} if caused by an increase in less negative (relatively ^2H-enriched) spring-summer precipitation (see Fig. 1c).

We interpret the shift to more positive δ^2H_{aq} values after ~2150 cal. yr BP to reflect an increase in evaporative enrichment of the lake water during this time. The observed positive shift in δ^2H_{aq} values, as well as their ^2H-enrichment relative to $\delta2Hter$, are both characteristic of basins with a negative water balance[20,47]. As noted (see setting and approach), evaporation is often an important source of water loss in closed (endorheic) basin lakes like Lake Diamond[63,64]. Because evaporative isotope enrichment can outweigh other environmental controls on δ^2H values in leaf waxes, and because the positive hydrogen isotope shift during the past two millennia (the Common Era) is only recorded in Diamond Lake by lipids derived from aquatic plants that track lake water[35], our interpretation provides an explanation for all of the observations without invoking unreasonable changes in temperature or the seasonality of precipitation. It also allays concerns that the incidental spills of glacial meltwater inferred by[29] left a detectable imprint: as this water source is ^2H-depleted[65], substantial input would result in isotope changes in the opposite direction of what we observe in our record.

Based on the strong seasonal link between meteoric δ^2H and temperature in South Georgia (Figs. 1c, 2b), and the tendency of terrestrial compounds to record precipitation δ^2H in small catchments like that of Lake Diamond[66], we infer that down-core δ^2H_{terr} values reflect temperature change. As seen in Fig. 6, this interpretation is supported by the fact that the most prominent feature of our δ^2H_{terr} record—a ~20‰ oscillation towards heavier
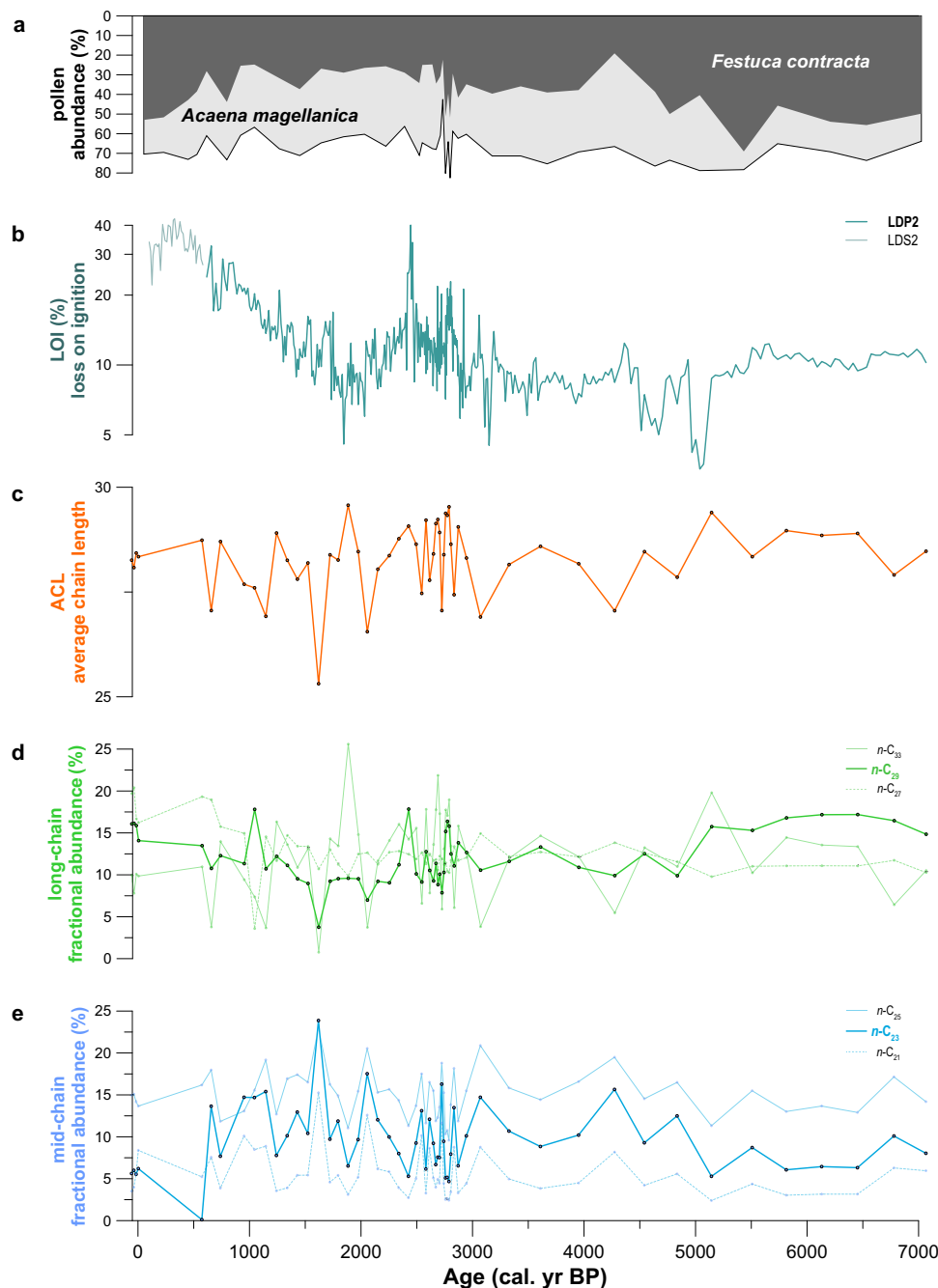
Fig. 3 Mid- to Late Holocene leaf wax distributions, pollen abundances, and organic content (LOI) in Lake Diamond. a Fractional abundances of mid-chain sedimentary n-alkanes, highlighting the predominantly aquatic C_{23} homolog. **b** Similar, but for long-chain compounds, highlighting terrestrially-sourced C_{29}. **c** The average chain length (ACL) distribution of down-core sedimentary n-alkane samples. **d** Variations in organic content as reflected by LOI measurements in both LDP2 and LDS2 cores. **e** A cumulative pollen diagram for core LDP2 after[60], highlighting the abundance of two taxa that have dominated local vegetation throughout the studied period: *Festuca* and *Acaena*.

isotopic values between 1200–600 cal. yr BP—coincides with warming phase South Georgia[27,30,60].

To quantify the impact of lake water evaporation through time, we calculate the isotopic difference between $\delta^2 H_{terr}$ (taken to reflect $\delta^2 H$ of precipitation) and $\delta^2 H_{aq}$ (taken to reflect $\delta^2 H$ of precipitation and evaporative enrichment of lake water) after[20], subtracting $\delta^2 H_{terr}$ from $\delta^2 H_{aq}$, and defining this parameter as $\varepsilon_{terr-aq}$. We chose the C_{29} and C_{23} n-alkanes to represent terrestrial and aquatic lipids, respectively, based on their maximum separation along PC2 (Fig. 5c), and use their $\delta^2 H$ values to calculate $\varepsilon_{terr-aq}$ change through time.

Due to core top sediment loss in LDP2 and extensive sub-sampling of LDS2[29], we have no measurements of $\delta^2 H_{terr}$ and $\delta^2 H_{aq}$ for the past 500 years (see Fig. 6). To extend our inferred evaporative enrichment reconstruction into this period, which overlaps with notable regional climate transitions including negative and positive phases of the Southern Annular Mode (SAM) and the culmination of the Little Ice Age (LIA)[12,67], we rely on proxy-to-proxy calibration[68]. Specifically, we use sediment organic content (measured by loss on ignition or LOI) as a substitute for measured $\varepsilon_{terr-aq}$ values during this interval (see methods), based on (1) statistically significant

($\rho = 0.66$, $p < 0.001$, $n = 14$) correspondence between these measurements (Fig. 7 and methods section) and (2) available LOI data from surface core LDS2 (Fig. 3b). We cannot be certain why this strong link between LOI and $\varepsilon_{terr-aq}$ exists, but widespread evidence for contemporaneous climate deterioration argues against an increase in lake productivity (Fig. 6a, c)[27,69]. Vegetation change also seems an unlikely culprit, as the previously discussed pollen evidence from Lake Diamond reveals that Holocene variability was minimal and unrelated to measured δD values (see section 2.1, and Figs. 3a, 5b). Finally, the non-significant anti-correlation
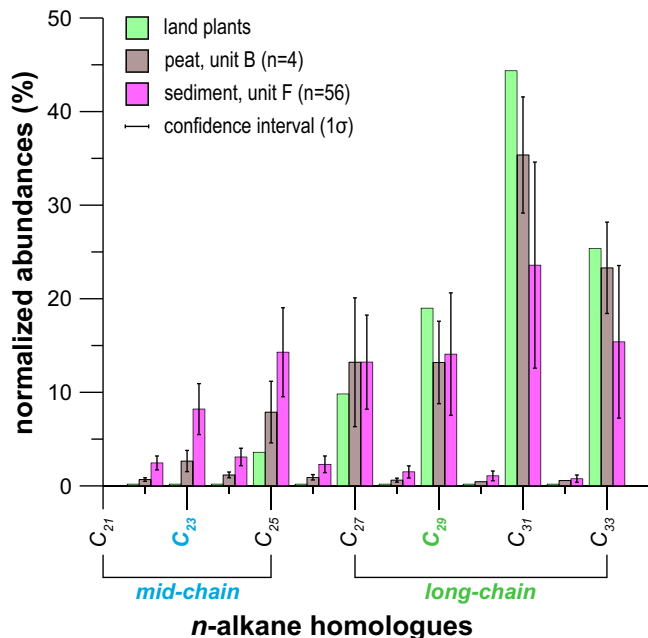
($R^2 = -0.03$) between LOI and the mass-specific magnetic susceptibility (χbulk)-derived glacier reconstruction by[29] allays concerns about the imprint of dilution with glacigenic clastic input during the investigated period. We hypothesize that the correlation between LOI and δ^2H_{aq} values can be attributed to the impact of inferred lake evaporation on water levels: particularly in a shallow and conically-shaped basin like Lake Diamond[29], low stands focus organic deposition into the center where our cores were extracted[70]. In support of this hypothesis, we also observe a strong ($\rho = -0.52$, $p < 0.05$, $n = 13$) correspondence in LDP2 between $\varepsilon_{terr-aq}$ and *Pediastrum* (Fig. 7)[60]. The abundance of this green algae genus is widely used as an indicator of lake level shallowing[71], also in upwind southern Patagonia[72]. As *Pediastrum* synthesizes some mid-chain *n*-alkanes[73], we should re-iterate that there is no relation between the abundance and isotopic value of these homologs in Lake Diamond (Fig. 5a).

Wind-driven evaporation during the past two millennia. We propose the inferred increase in evaporative water loss from Lake Diamond after ~2150 cal. yr BP was driven by strengthening winds. The previously discussed evidence for local and regional cooling at this time rules out direct temperature effects (Fig. 6a)[27,44,61]. We also reject decreasing relative humidity as an explanation because such a change would be reflected by an increase in δ^2H_{ter} values due to leaf water enrichment[48], which we do not observe (Fig. 6b). Our interpretation is supported by macrofossil evidence from peatlands, sensitive archives of sub-Antarctic surface water balance[74,75], which reveal a sharp transition ~2200 cal. yr BP towards colder wetter (humid) conditions in South Georgia (Fig. 6c).

Variations in wind strength can leave a measurable isotopic imprint on closed (endorheic) basins in the SWH core belt like Lake Diamond[76]. Nearby paleoclimate records indicate that wind strength indeed increased after ~2150 cal. yr BP, when $\varepsilon_{terr-aq}$ began to deviate. A record from neighboring Annenkov Island shows an increase in the accumulation rates of long-distance transported (LDT) pollen—an established indicator of wind strength[77,78]. Further upwind (52.5°S and 72.6°W), close to the Andean crest, where strengthening of the westerlies is coupled to an increase in orographic precipitation[79], the amount of hygrophytic pollen increased throughout the last two millennia[80]. A similar trend is observed in upwind Lago Guanaco (51.5°S and

Fig. 4 Chain-length distributions. The abundance of *n*-alkane homologs in terrestrial plants collected in South Georgia by ref. [54], and sediment and peat samples from the investigated archive from Lake Diamond (LDP2). We distinguish between mid- and long-chain compounds after the definition by ref. [49] in color coding that corresponds with Figs. 3, 5, 6. Confidence intervals are based on down-core variations of LDP2 samples (see Fig. 6).
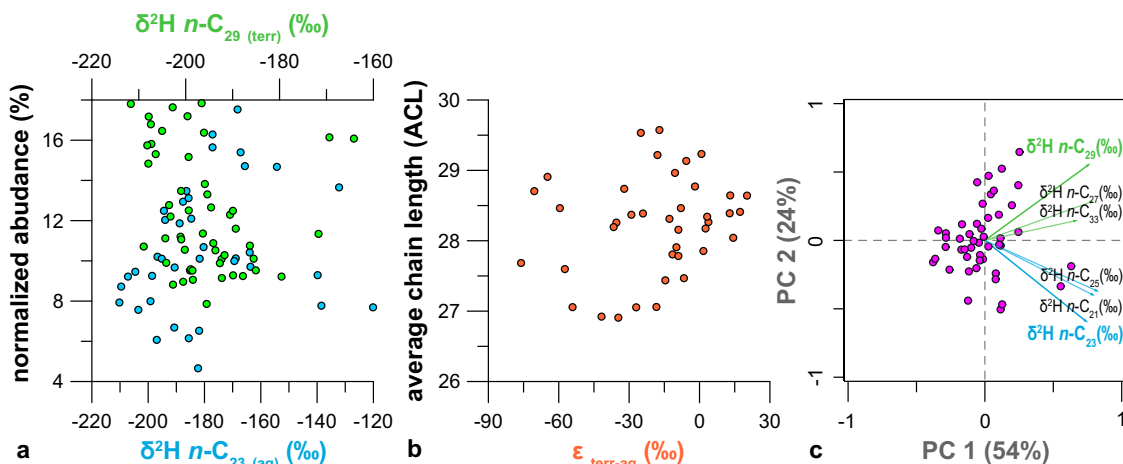

Fig. 5 Relations between *n*-alkane chain length and isotope values. Bi-plots showing **a** The hydrogen isotope (δ^2H) composition of representative mid-(C_{23}) and long-chain (C_{29}) sedimentary *n*-alkane sample combinations versus their normalized abundance, **b** The isotopic offset between compounds produced by representative aquatic (C_{23}) and terrestrial (C_{29}) plants ($\varepsilon_{terr-aq}$) versus the Average Chain Length (ACL) of all alkanes measured in these samples ($n = 39$), and **c** Sample (pink dots) and variable (vectors) scores for the main ordination axes (PC 1–2: labeled with their explanatory power) of principal component analysis (PCA) carried out on measured δ^2H values of analyzed *n*-alkanes (*n*-C_{21} to *n*-C_{33} without *n*-C_{31}: see methods section).
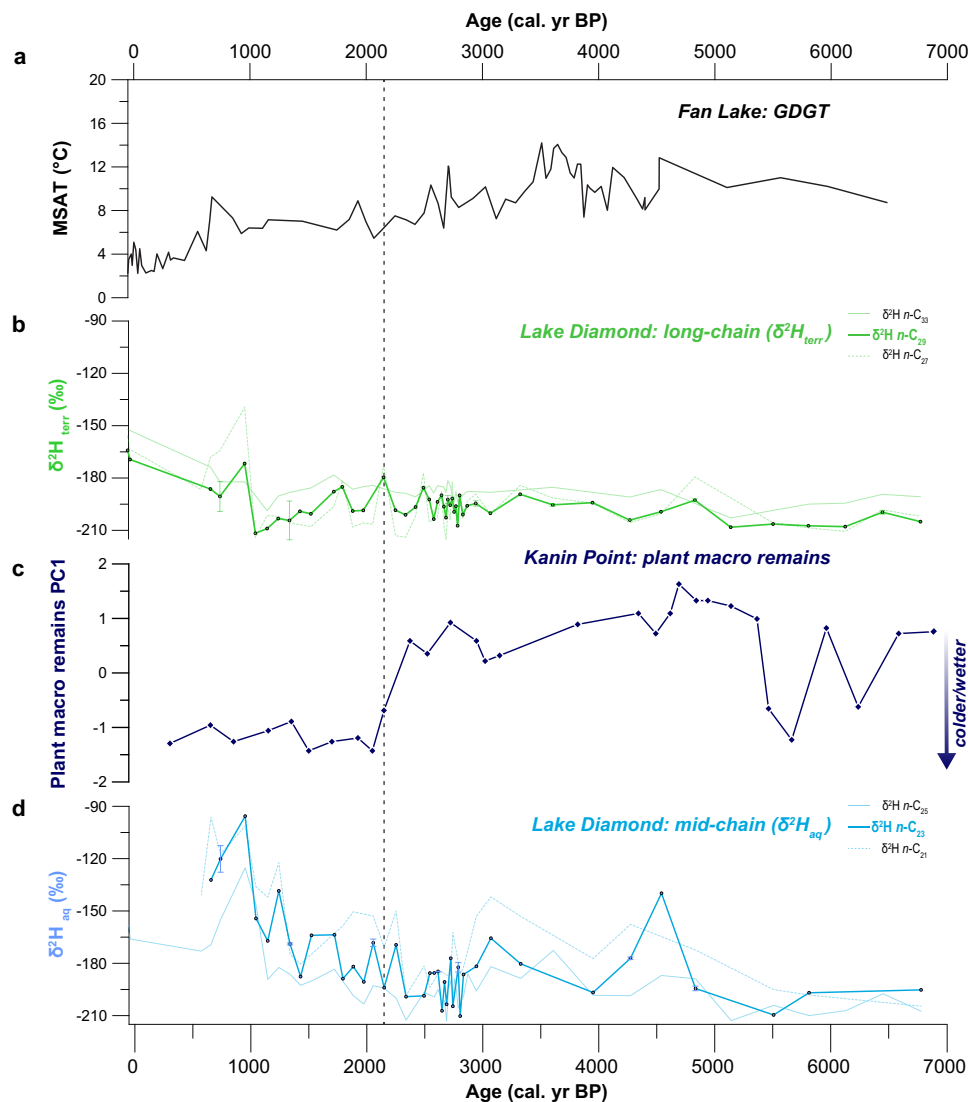
Fig. 6 Comparing compound-specific hydrogen isotope values (δ2H) from Lake Diamond with local temperature and hydroclimate proxies. a GDGT-derived mean summer air temperatures (MSAT) from neighboring Annenkov Island[27]. **b** Terrestrially produced long-chain *n*-alkane δ2H values from Lake Diamond (this study), highlighting representative C29 homolog. **c** Principal component analysis (PCA) of plant macrofossil data from ref. [69]. **d** Aquatically sourced short-chain *n*-alkane δ2H values from Lake Diamond (this study), highlighting representative C23 homolog. The ~2150 cal. yr BP age where change-point analysis detects a significant deviation from the long-term mean is shown by a stippled line. All color coding matches that of Figs. 3–6.

72.5 °W), where (1) a carbonate-derived δ18O-based reconstruction of the balance between wind-driven precipitation and surface evaporation from Lago Guanaco is similar (ρ = 0.53, *p* < 0.001, *n* = 35) to our inferred wind-driven evaporation record from Lake Diamond during the overlapping ~100–950 cal. yr BP period (Fig. 8)[21], and (2) gradual wind-driven precipitation increases during this period are reflected by the dominance of forest over grassland[40] (Fig. 9d). We attribute the delayed response of the latter transition to the well-documented nonlinear relation between regional changes in vegetation and climate[19].

Links to the southern annular mode (SAM). The Lake Diamond εterr-aq wind-driven lake evaporation reconstruction suggests that the past two millennia were characterized by major regional shifts in core belt SHW strength that appears unmatched in the past 7 ka. As seen in Figs. 8, 9, the transition towards windier conditions seems to mark a major reorganization of the regional climate system as the pattern of change observed in Lake Diamond broadly coincides with (1) pronounced annual cooling towards a

post-glacial temperature minimum off the northeastern Antarctic Peninsula (Fig. 9b)—recorded by ice core δ2H values from James Ross Island (Fig. 1a) and (2) extension of the sea ice season towards a Holocene maximum along the western Antarctic Peninsula (Fig. 9c) as indicated by a rise in sea ice diatom bio-marker concentrations[81]. A concomitant increase in seabird-derived phosphorus (P) from a rookery on the Falklands also attests to the broad ecological impacts of these climatic changes (Fig. 9e)[82]. Sea ice cover and wind stress have a major impact on the sub-Antarctic food web through impacts on the transport of nutrient waters as well as productivity and feeding[83,84]. This reconstructed pattern of coupled cooling, mid-latitude westerly intensification, and the Bellingshausen Sea ice expansion is diagnostic for a negative phase of the Southern Annular Mode or SAM[12,85,86]. The SAM is the main pattern of Southern Ocean climate variability[9] and affects the strength and position of the SHW by modulating the atmospheric pressure gradient between 40–65°S (see introduction). There is a strong correlation (Spearman's correlation coefficient ρ = 0.75, *p* < 0.0001, *n* = 35) between our inferred evaporation record and the sole annual
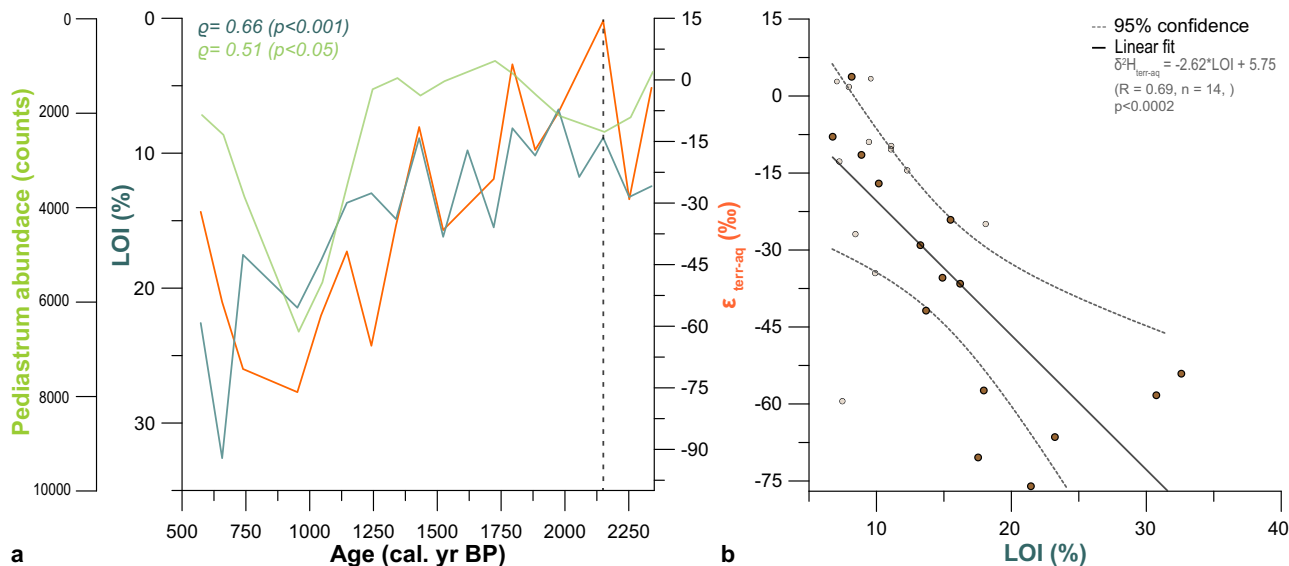
Fig. 7 Proxy-to-proxy calibration. a $\varepsilon_{terr-aq}$ and LOI values, as well as *Pediastrum* counts from ref. [60] in core LDP2 over the past two millennia (unit F3: see methods) and **b** A bi-plot for this period that captures the association between these parameters with a linear regression fit (opaque dots) and shows how data from the preceding 2.4–7 ka BP period covered by LDP2 (transparent dots) relate to this model (also see methods). For the latter purpose, we excluded values ($n = 7$) from the ~2.4–2.7 ka BP to avoid closed-sum effects from dilution with alluvial clastic input during this time, as reported by ref. [29].
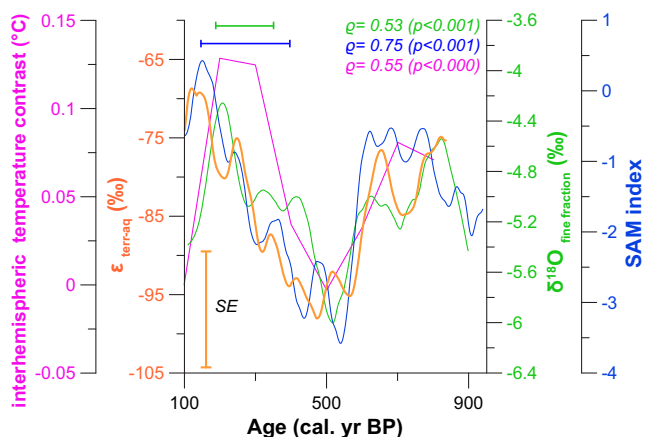

Fig. 8 Comparing inferred $\varepsilon_{terr-aq}$ values from Lake Diamond (orange) with other regional proxies of wind-driven change. In blue, the Southern Annular Mode (SAM) index by ref. [12]. And in green, the $\delta^{18}O$ fine fraction SHW record from Lago Guanaco by ref. [21]. Shown in purple is the area-weighted inter-hemispheric temperature contrast between the extratropics (30–90°) of both hemispheres (North-South) using 30° averages of ensemble means presented by ref. [110]. All reconstructions have been smoothed using a 70-year moving average. In the upper part of the figure, we show chronological uncertainties (horizontal bars) and correlation coefficients (italics) in matching colors. The vertical bar at the base marks the reported standard error (SE) of our PTP-derived model (see methods).

SAM reconstruction that extends back to 1000 CE, demonstrating that Lake Diamond sediments indeed capture shifts in the behavior of this dominant regional climate mode (Fig. 8)[12]. These also include the positive SAM trend—characterized by less windy conditions over Lake Diamond—during the past 500 years. We thus argue that our reconstruction of wind-driven evaporation is linked to SAM variability over the past 7 millennia. However, to acknowledge that links with SHW strength (1) depend on the choice of index and reanalysis data[22], and (2) could be non-stationary through time[13], we refer to SAM-like changes in the following paragraphs after[85]. Concretely, we define these as

changes in wind-driven evaporation that were likely driven by shifts in the meridional pressure gradient.

Positive modern SAM phasing was not unprecedented during Holocene. The Lake Diamond record provides valuable information concerning long-term SAM behavior. Notably, the period from 7 ka BP until ~2150 cal. yr BP was comparatively stable and mostly characterized by positive SAM-like conditions (Fig. 9). Based on baseline data that do not extend beyond the past millennium[13], it has been argued that today's positive SAM phasing—is attributed to a combination of anthropogenic greenhouse forcing and ozone depletion[11,87]—falls outside the range of natural variability[8]. Our findings indicate that this may not be the case and that the negative SAM polarity of the past two millennia was exceptional rather than today's positive phasing. While acknowledging the possibility that the relation between wind-driven evaporation in Lake Diamond and the SAM is non-stationary beyond the past millennium[13], we use the relationship ($R^2 = 0.65$, $p = 0.000$) between the Lake Diamond data and the SAM index by[12] to approximate modern limits. Based on this basic calculation, we find that $\varepsilon_{terr-aq}$ values greater than $-45‰$ exceed the observed 1999 CE SAM maximum (Fig. 9a). Notwithstanding the uncertainties of this simple approach, it highlights that SAM values have been near or exceeded observational limits during most of the Mid- to Late Holocene, and underscores the potential of this period to better understand the impacts of a more positive SAM, which is predicted for the future[87]. Our findings corroborate previous proxy-derived evidence that strongly positive SAM phases do not require anthropogenic radiative forcing[13,85]. Taken together, this body of work hints at the possibility that internal variations, which will be superimposed on future anthropogenic change but remain poorly resolved in climate models[87], play a critical but undervalued role in driving SAM shifts.

Was SAM-like change driven by Northern Hemisphere cooling? In the following discussion, we examine whether the multi-centennial Common Era climate variations captured by the Lake Diamond record and other reconstructions of SAM-like change in
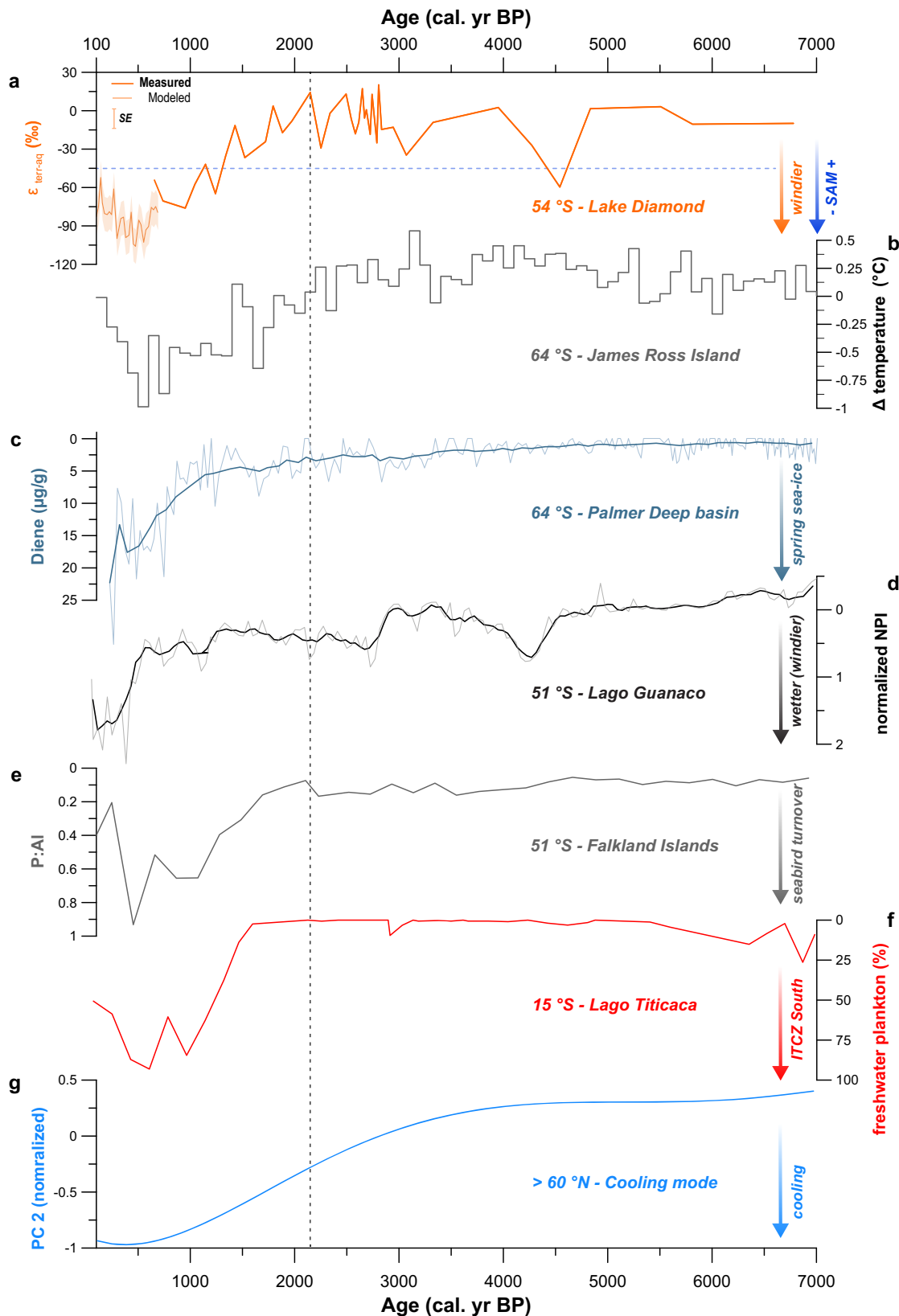
Fig. 9 could have been caused by modes of internal variability. Specifically, the El Niño-southern oscillation or ENSO[14]. El Niño events are associated with negative SAM phases because positive temperature anomalies in the Tropical Pacific trigger Rossby wave trains that propagate positive pressure differences poleward[88]. Conversely, La Niña events coincide with positive SAM phases as ensuing Tropical Pacific cooling leads to low sea-level pressure anomalies in the sub-Antarctic. Recently, it has been shown that these connections also operate on centennial timescales[17]. However, while the reconstructed SAM minimum ~500 cal. yr BP (Fig. 8) coincides with a phase of El Niño-dominated conditions[89], no consistent link exists between records of SAM-like variability

Fig. 9 Comparing evaporation in Lake Diamond with regional proxies of sea ice, wind, seabird, and temperature shifts. a Lake Diamond $\varepsilon_{terr-aq}$ values. Please note that we distinguish between reconstructed and PTP-inferred values (see methods), while also displaying the SE of this model. **b** James Ross Island (JRI) ice core temperature reconstruction after[44], showing 100-year averaged anomalies compared to the CE 1961–1990 mean. **c** Diatom-derived di-unsaturated (diene) highly branched isoprenoid (HBI) biomarker concentrations from[81]. **d** Raw and smoothed standardized *Nothofagus* (southern beech tree)/Poaceae (grass) Index (NPI) values from[40]. **e** Seabird-derived ratios of bio-element Phosphorus (P) over lithogenic Aluminum (Al) after[82]. **f** Freshwater plankton abundances (%) in Lake Titicaca from[104]. **g** Normalized smoothed principal component 2 (PC2) values of the global cooling mode inferred by ref. [109].

and ENSO reconstructions[90]. Indeed, there is growing consensus that ENSO-SAM links are non-stationary[13,91], and also depend on the strength of the latter[92]. In light of this evidence, we note that the Common Era excursion captured in the Lake Diamond record and the other records of SAM-like change in Fig. 9 coincides with the onset of ENSO strengthening to a Holocene maximum[93,94]. Such long-term trends are, however, often characterized as ENSO-like and attributed to other mechanisms that likewise affect tropical Pacific surface temperature change[88].

There is, for example, mounting evidence for a global atmospheric teleconnection that is (1) considered analogous to ENSO as it also impacts equatorial convection, but (2) driven by the temperature gradient between Earth's hemispheres, and (3) operating at the multi-centennial timescales resolved by our record[95]. The emerging observational, model-based, and proxy-derived evidence supporting this framework shows that differential extratropical temperature change increases poleward heat export to the cooler hemisphere[96–98]. To facilitate this, the inter-tropical convergence zone (ITCZ) moves into the warmer hemisphere so that more energy is transported across the equator[99,100]. A similar response is observed during ENSO variations as the ITCZ migrates south into a warming South Pacific during El Niño events and vice versa during La Niña[101]. Critically, model experiments reveal that this feedback also alters the strength and position of the core SHW belt through poleward Rossby wave train propagation[102]—a key characteristic of modern ENSO-SAM interactions[88].

To assess whether this global atmospheric teleconnection may help explain the Common Era excursion observed in our isotope record and the other reconstructions of SAM-like change shown in Fig. 9, we focus on anticipated changes in ITCZ position and meridional temperature gradient[95]. In light of the presented shift towards anomalously negative SAM values (Figs. 8, 9a), and the association of this state with El Niño-like (negative ENSO) conditions[88], these include evidence for a southward ITCZ migration in response to Northern Hemisphere cooling or Southern Hemisphere warming. Proxy evidence from the sensitive southern limit (15°S) of the present-day South American ITCZ reveals major contemporaneous precipitation increases—the main expression of such a shift[103]. As seen in Fig. 9f, this is recorded by a sharp increase in freshwater plankton abundances in oligohaline Lake Titicaca from 2 ka BP onwards[104]. A transition from dry savanna to a wetter rain forest, reflected by a sharp rise in *Moraceae* (mulberry) pollen ~2160 cal. yr BP in southern Amazonia (13–14°S)[105] also supports this interpretation. Both observations are in broad agreement with global evidence for a southward ITCZ migration during the Late Holocene in response to orbitally-driven Northern Hemisphere cooling[96,106]. This trend was amplified during the last two millennia by the negative radiative effects of Arctic sea ice expansion[107] and is identified as one of the major temperature shifts of the Holocene[108]. Recent proxy-validated simulations even identify this feedback as the main driver of global temperature change during the Common Era[109].

As seen in Fig. 9g, the evolution of this cooling mode tracks the millennial-scale trend of mid to late Holocene SAM-like

variability in our study region and shows that cooling rates intensify around ~2100 cal. yr BP. To further investigate the correspondence between the Common Era SAM-like changes discussed here and (relative) Northern Hemisphere cooling, we compare our Lake Diamond reconstruction and the millennium-long SAM index of[12] to the temperature contrast between the extratropics (30–90°) of both hemispheres (North minus South) —a measure of Earth's meridional temperature gradient. To do so, we rely on the area-weighted ensemble means of the 30° latitude average presented by[110]. Figure 8 underlines that the Northern Hemisphere cooled differentially during this period and reveals a notable degree of agreement ($\rho = 0.55$, $p < 0.000$, $n = 22$) with coeval SAM-like changes.

Following the above, we argue that the inferred shift towards a negative SAM-like state after ~2150 cal. yr BP is consistent with a change in Earth's thermal gradient in response to amplified Arctic cooling. Our findings thus provide additional evidence for the existence of a previously hypothesized atmospheric teleconnection that links the high latitudes in both hemispheres and impacts SHW strength[88]. This raises the possibility that ongoing amplified Arctic warming may (1) reinforce the predicted trend towards a more positive phase of SAM[87] and (2) impact the ability of the SHW to help regulate the global climate in the future.

Methods

Biomarker analysis. In total, 56 samples were extracted from the lacustrine sequence of piston core LDP2 ($n = 52$) and surface core LDS2 ($n = 4$) at 2–4 cm intervals. In addition, we analyzed five samples from the underlying peat deposit in LDP2. Prior to analysis, these sediments were homogenized and freeze-dried. We extracted lipids from each sample with a 9:1 v/v solution of dichloromethane (DCM) and methanol using a Dionex 350 Accelerated Solvent Extractor. The Total Lipid Extract (TLE) that was obtained was then dried under a stream of nitrogen gas in a Biotage TurboVap. Next, TLEs were separated into aliphatic, ketone, and polar fractions using silica gel flash column chromatography. For this purpose, we sequentially used four bed volumes of hexane, DCM, and methanol as eluents. Aliphatic compounds were then treated with copper to remove elemental sulfur and eluted through silver nitrate-impregnated silica gel to remove unsaturated hydrocarbons. We subsequently identified and quantified C_{21}–C_{33} *n*-alkanes in the saturated fraction following the protocol outlined by ref. [111] and by comparing sample mass spectra to a drift standard containing homologous *n*-alkanes (C_8–C_{40}), phytane, pristane, and 5α-androstane. Measurements were made using the protocol by ref. [111] on an Agilent 7890 gas chromatograph (GC) equipped with both mass selective (MSD) and flame ionization (FID) detectors, as well as an HP-5ms column. Average Chain Lengths (ACL) were determined[112]:

$$ACL = \sum(C_i)(X_i)/\sum(C_i), \qquad (1)$$

where C is the concentration and X is the chain length of *n*-alkane i.

Hydrogen isotope measurements of these homologs were performed on a Thermo Trace GC coupled to a Thermo Delta V Isotope Ratio Mass Spectrometer (IRMS) via an Isolink Conflo IV interface using the same column and protocol by ref. [111] as for GC-MSD/FID analysis. Based on chromatographic evidence of co-elution with a hopanoid compound, we excluded *n*-C_{31} isotope ratios from our record. Most compounds were measured in triplicate, and the precision of replicate measurements was typically better than 2.5‰ (1σ). Measurements with intensities lower than 1000 mV on mass two were excluded. To monitor analytical uncertainty, an external transesterified *n*-alkanoic acid mixture calibrated against authenticated A4 and F8 lipid mixtures—provided by A. Schimmelmann from the University of Indiana—was measured after every sixth sample. Throughout the analysis, precision ranged from 0.95 to 2.4‰ among four homologs. To convert compound-specific δ^2H values to the VSMOW scale after[113], we regularly measured the authenticated A5 lipid mixture— provided by A. Schimmelmann from the University of Indiana. We also report the δ^2H offset between terrestrially-sourced *n*-C_{29} and aquatically produced *n*-C_{23} ($\varepsilon_{terr-aq}$) after[114].

Core stratigraphy. The stratigraphy of the presented Lake Diamond record is described in detail by ref. [29]. As stated before, our analysis prioritizes sediments deposited under lacustrine conditions. These encompass the upper 221.5 cm of piston core LDP2 that cover the past 7.2 ka[29]. subdivide this sequence into three lithological units: the compacted silt-dominated organic-rich sediments of unit D (194–221.5 cm), the poorly sorted sandy mass wasting deposit of unit E (185.5–194 cm) and the silty-sandy dark brown organic-rich deposits of unit F (0–185.5 cm). Here, we complement the multi-proxy dataset from[29] with palynological and loss-on-ignition (LOI) analyzes. To allow proxy-to-proxy calibration for the past 500 years—which are not covered by core LDP2[29]—we measured LOI at ~1 cm increments on sub-sectioned pollen samples from surface core LDS2 ($n = 35$). For this purpose, we extracted 0.5 ml of sediment with a syringe and dried it overnight at 105 °C before burning samples at 550 °C for 4 h after[115]. These data do not overlap with the observational period as the uppermost 6.5 cm (150 years) has been used for ^{210}Pb dating[60] and biomarker analysis. Pollen samples were analyzed at 4–10 cm intervals from the composite lake Diamond record ($n = 41$) as detailed by ref. [60]. Slide preparation was carried out using standard techniques after[116]. Eucalyptus tablets were added to calculate concentrations, while identification was aided by[117] and reference material collected during fieldwork in 2011 and 2015.

Geostatistics. We used basic predictive models to construct waterlines (Fig. 2a), constrain the controls on meteoric δ^2H (Fig. 2b), and substitute LOI for $\varepsilon_{\text{terr-aq}}$ (see Section 3.1 and Fig. 7b). For this purpose, the following linear ordinary least squares (OLS) regression curves were fitted with the help of Stata 16:

$$\delta^2\text{H} = 7.61 * \delta^{18}\text{O} + 0.84 \tag{2}$$

$$\delta^2\text{H} = 5.83 * T - 78.11 \tag{3}$$

$$\varepsilon_{\text{terr-aq}} = -2.62 * \text{LOI} + 5.75 \tag{4}$$

To avoid artifacts stemming from autocorrelation[68], we relied on the Durbin–Watson d statistic using 1.5 and 2.5 as cut-off values following the recommendations of ref. [118]. Proxy-to-proxy calibration of $\varepsilon_{\text{terr-aq}}$ against LOI focused on the upper part of LDP2, where both datasets significantly deviate from a stable long-term mean (see section 2.1 and Fig. 7a). To pinpoint this transition, we relied on change-point analysis using the cpt.mean function and AMOC method in version 2.2.2 of the change-point R package[119]. The detected change-point at 60 cm (~2150 cal. yr BP) core depth corresponds to the transition into unit F4[29]. We did not incorporate include data from underlying unit F3 to avoid closed-sum effects from dilution with alluvial clastic input deposited in this interval as reported by[29]. We do, however, show how $\varepsilon_{\text{terr-aq}}$—LOI combinations from this preceding 2.4–7 ka BP period covered by LDP2 relate to equation 5 in Fig. 7b. Finally, we carried out a principal component analysis (PCA) on samples ($n = 49$) where δ^2H was measured at least once on each homolog (n-C21 to n-C33 without n-C31: see biomarker analysis) to evaluate the degree of co-variance between compounds (see section 2.1 and Fig. 4c). To do so, we used version 5 of the Canoco software[120]. Following the recommendations of ref. [121], all n-alkane homologs were centered and standardized prior to analysis.

Data availability
The authors declare that all data that we generated for this study and are presented in the figures of this manuscript are available in Supplementary Data 1 and have been uploaded to the DataverseNO repository. Here, the files can be accessed using the following DOI - https://doi.org/10.18710/IYNKEZ.

References
1. Sabine, C. L. et al. The oceanic sink for anthropogenic CO2. *science* **305**, 367–371 (2004).
2. Frölicher, T. L. et al. Dominance of the Southern Ocean in anthropogenic carbon and heat uptake in CMIP5 models. *J. Clim.* **28**, 862–886 (2015).
3. Marshall, J. & Speer, K. Closure of the meridional overturning circulation through Southern Ocean upwelling. *Nat. Geosci.* **5**, 171–180 (2012).
4. Lovenduski, N. S., Gruber, N. & Doney S. C. Toward a mechanistic understanding of the decadal trends in the Southern Ocean carbon sink. *Glob. Biogeochem. Cycles* **22** (2008).
5. Hodgson, D. A. & Sime, L. C. Southern westerlies and CO 2. *Nat. Geosci.* **3**, 666–667 (2010).
6. Le Quéré, C. et al. Saturation of the Southern Ocean CO2 sink due to recent climate change. *Science* **316**, 1735–1738 (2007).
7. Gong, D. & Wang, S. Antarctic oscillation: concept and applications. *Chin. Sci. Bull.* **43**, 734–738 (1998).
8. Fogt, R. L. & Marshall, G. J. The Southern Annular Mode: variability, trends, and climate impacts across the Southern Hemisphere. *Wiley Interdisc. Rev. Clim. Change* **11**, e652 (2020).
9. Marshall, G. J. Trends in the Southern Annular Mode from observations and reanalyses. *J. Clim.* **16**, 4134–4143 (2003).
10. Gillett, N. P., Kell, T. D. & Jones, P. Regional climate impacts of the Southern Annular Mode. *Geophys. Res. Lett.* **33** (2006).
11. Thompson, D. W. et al. Signatures of the Antarctic ozone hole in Southern Hemisphere surface climate change. *Nat. Geosc.* **4**, 741–749 (2011).
12. Abram, N. J. et al. Evolution of the Southern Annular Mode during the past millennium. *Nat. Clim. Change* **4**, 564–569 (2014).
13. Dätwyler, C. et al. Teleconnection stationarity, variability and trends of the Southern Annular Mode (SAM) during the last millennium. *Clim. Dyn.* **51**, 2321–2339 (2018).
14. Fogt, R. L., Bromwich, D. H. & Hines, K. M. Understanding the SAM influence on the South Pacific ENSO teleconnection. *Clim. Dyn.* **36**, 1555–1576 (2011).
15. Ding, Q., Steig, E. J., Battisti, D. S. & Wallace, J. M. Influence of the tropics on the Southern Annular Mode. *J. Clim.* **25**, 6330–6348 (2012).
16. Wang, G. & Cai, W. Climate-change impact on the 20th-century relationship between the Southern Annular Mode and global mean temperature. *Sci. Rep.* **3**, 1–6 (2013).
17. Dätwyler, C., Grosjean, M., Steiger, N. J. & Neukom, R. Teleconnections and relationship between the El Niño–Southern Oscillation (ENSO) and the Southern Annular Mode (SAM) in reconstructions and models over the past millennium. *Clim. Past* **16**, 743–756 (2020).
18. Saunders, K. M. et al. Holocene dynamics of the Southern Hemisphere westerly winds and possible links to CO 2 outgassing. *Nat. Geosci.* **11**, 650–655 (2018).
19. Kilian, R. & Lamy, F. A review of Glacial and Holocene paleoclimate records from southernmost Patagonia (49–55 S). *Quat. Sci. Rev.* **53**, 1–23 (2012).
20. Mügler, I. et al. Effect of lake evaporation on δD values of lacustrine n-alkanes: A comparison of Nam Co (Tibetan Plateau) and Holzmaar (Germany). *Org. Geochem.* **39**, 711–729 (2008).
21. Moy, C. M. et al. Isotopic evidence for hydrologic change related to the westerlies in SW Patagonia, Chile, during the last millennium. *Quat. Sci. Rev.* **27**, 1335–1349 (2008).
22. Ho, M., Kiem, A. & Verdon-Kidd, D. The Southern Annular Mode: a comparison of indices. *Hydrol. Earth Syst. Sci.* **16**, 967–982 (2012).
23. Trouet, V. & Van Oldenborgh, G. J. KNMI Climate Explorer: a web-based research tool for high-resolution paleoclimatology. *Tree-Ring Res.* **69**, 3–13 (2013).
24. Fogt, R. L. et al. Historical SAM variability. Part II: twentieth-century variability and trends from reconstructions, observations, and the IPCC AR4 models. *J. Clim.* **22**, 5346–5365 (2009).
25. Clapperton, C. M., Sugden, D. E., Birnie, J. & Wilson, M. J. Late-glacial and Holocene glacier fluctuations and environmental change on South Georgia, Southern Ocean. *Quat. Res.* **31**, 210–228 (1989).
26. Bakke, J., Paasche, Ø., Schaefer, J. M. & Timmermann, A. Long-term demise of sub-Antarctic glaciers modulated by the Southern Hemisphere Westerlies. *Sci. Rep.* **11**, 1–10 (2021).
27. Foster, L. C. et al. Development of a regional glycerol dialkyl glycerol tetraether (GDGT)–temperature calibration for Antarctic and sub-Antarctic lakes. *Earth Planet. Sci. Lett.* **433**, 370–379 (2016).
28. Gordon, J. E., Haynes, V. M. & Hubbard, A. Recent glacier changes and climate trends on South Georgia. *Glob. Planet. Change* **60**, 72–84 (2008).
29. Oppedal, L. T., Bakke, J., Paasche, Ø, Werner, J. P. & van der Bilt, W. G. M. Cirque glacier on South Georgia shows centennial variability over the last 7000 years. *Front. Earth Sci.* (2018).
30. Strother, S. L. et al. Changes in Holocene climate and the intensity of Southern Hemisphere Westerly Winds based on a high-resolution palynological record from sub-Antarctic South Georgia. *The Holocene* **25**, 263–279 (2015).
31. van der Bilt, W. G. M. et al. Late Holocene glacier reconstruction reveals retreat behind present limits and two-stage Little Ice Age on subantarctic South Georgia. *J. Quat. Sci.* **32**, 888–901 (2017).
32. Xia, Z., Oppedal, L. T., Van der Putten, N., Bakke, J. & Yu, Z. Ecological response of a glacier-fed peatland to late Holocene climate and glacier changes on subantarctic South Georgia. *Quat. Sci. Rev.* **250**, 106679 (2020).
33. ESA, EC. *Copernicus Sentinel 2* (2016).
34. Castañeda, I. S. & Schouten, S. A review of molecular organic proxies for examining modern and ancient lacustrine environments. *Quat. Sci. Rev.* **30**, 2851–2891 (2011).
35. Sachse, D. et al. Molecular paleohydrology: interpreting the hydrogen-isotopic composition of lipid biomarkers from photosynthesizing organisms. *Ann. Rev. Earth Planet. Sci.* **40**, 221–249 (2012).

36. Sessions, A. L., Burgoyne, T. W., Schimmelmann, A. & Hayes, J. M. Fractionation of hydrogen isotopes in lipid biosynthesis. *Org. Geochem.* **30**, 1193–1200 (1999).

37. Sternberg LdSL. D/H ratios of environmental water recorded by D/H ratios of plant lipids. *Nature* **333**, 59 (1988).

38. Dansgaard, W. Stable isotopes in precipitation. *Tellus* **16**, 436–468 (1964).

39. Garreaud, R. D. Precipitation and circulation covariability in the extratropics. *J. Climate* **20**, 4789–4797 (2007).

40. Moreno, P., Francois, J., Moy, C. & Villa-Martínez, R. Covariability of the Southern Westerlies and atmospheric CO2 during the Holocene. *Geology* **38**, 727–730 (2010).

41. Thomas, Z. et al. A new daily observational record from Grytviken, South Georgia: exploring twentieth-century extremes in the South Atlantic. *J. Climate* **31**, 1743–1755 (2018).

42. Bowen G. The online isotopes in precipitation calculator, version 3.1. (2019).

43. Abram, N. J., Mulvaney, R. & Arrowsmith, C. Environmental signals in a highly resolved ice core from James Ross Island, Antarctica. *J. Geophys. Res. Atm.* **116**, 1-15 (2011).

44. Mulvaney, R. et al. Recent Antarctic Peninsula warming relative to Holocene climate and ice-shelf history. *Nature* **489**, 141–144 (2012).

45. IAEA/WMO. Global network of isotopes in precipitation. The GNIP Database. 2020. http://www.iaea.org/water.

46. Brinkmann, N. et al. Employing stable isotopes to determine the residence times of soil water and the temporal origin of water taken up by Fagus sylvatica and Picea abies in a temperate forest. *New Phytolo.* **219**, 1300–1313 (2018).

47. Balascio, N. L., D'Andrea, W. J., Bradley, R. S. & Perren, B. B. Biogeochemical evidence for hydrologic changes during the Holocene in a lake sediment record from southeast Greenland. *The Holocene* **23**, 1428–1439 (2013).

48. Kahmen, A., Schefuß, E. & Sachse, D. Leaf water deuterium enrichment shapes leaf wax n-alkane δD values of angiosperm plants I: Experimental evidence and mechanistic insights. *Geochim. Cosmochim. Acta* **111**, 39–49 (2013).

49. Ficken, K. J., Li, B., Swain, D. L. & Eglinton, G. An n-alkane proxy for the sedimentary input of submerged/floating freshwater aquatic macrophytes. *Org. Geochem.* **31**, 745–749 (2000).

50. Meyers, P. A. Applications of organic geochemistry to paleolimnological reconstructions: a summary of examples from the Laurentian Great Lakes. *Org. Geochem.* **34**, 261–289 (2003).

51. Diefendorf, A. F. & Freimuth, E. J. Extracting the most from terrestrial plant-derived n-alkyl lipids and their carbon isotopes from the sedimentary record: a review. *Org. Geochem.* **103**, 1–21 (2017).

52. Dion-Kirschner, H., McFarlin, J. M., Masterson, A. L., Axford, Y. & Osburn, M. R. Modern constraints on the sources and climate signals recorded by sedimentary plant waxes in west Greenland. *Geochim. Cosmochim. Acta* **286**, 336–354 (2020).

53. McFarlin, J. M., Axford, Y., Masterson, A. L. & Osburn, M. R. Calibration of modern sedimentary δ2H plant wax-water relationships in Greenland lakes. *Quat. Sci. Rev.* **225**, 105978 (2019).

54. Mackie, P. R., Platt, H. M. & Hardy, R. Hydrocarbons in the marine environment: II. Distribution of n-alkanes in the fauna and environment of the sub-antarctic island of South Georgia. *Estuar. Coastal Marine Sci.* **6**, 301–313 (1978).

55. Hockun, K. et al. Using distributions and stable isotopes of n-alkanes to disentangle organic matter contributions to sediments of Laguna Potrok Aike, Argentina. *Org. Geochem.* **102**, 110–119 (2016).

56. Nichols, J. E., Booth, R. K., Jackson, S. T., Pendall, E. G. & Huang, Y. Paleohydrologic reconstruction based on n-alkane distributions in ombrotrophic peat. *Org. Geochem.* **37**, 1505–1513 (2006).

57. Bush, R. T. & McInerney, F. A. Leaf wax n-alkane distributions in and across modern plants: implications for paleoecology and chemotaxonomy. *Geochim. Cosmochim. Acta* **117**, 161–179 (2013).

58. Balascio, N. L., D'Andrea, W. J., Anderson, R. S. & Wickler, S. Influence of vegetation type on n-alkane composition and hydrogen isotope values from a high latitude ombrotrophic bog. *Org. Geochem.* **121**, 48–57 (2018).

59. Polissar, P. J. & Freeman, K. H. Effects of aridity and vegetation on plant-wax δD in modern lake sediments. *Geoch. Cosmochim. Acta* **74**, 5785–5797 (2010).

60. Zwier M., van der Bilt, W. G. M., de Stigter, H. & Bjune A. E. Pollen evidence of variations in Holocene climate and Southern Hemisphere Westerly Wind strength on sub-Antarctic South Georgia. *The Holocene*, **12** (2021).

61. Roberts, S. J. et al. Past penguin colony responses to explosive volcanism on the Antarctic Peninsula. *Nat. Commun.* **8**, 1–16 (2017).

62. Cooper, L. et al. Stable isotopes of oxygen and natural and fallout radionuclides used for tracing runoff during snowmelt in an Arctic watershed. *Water Resour. Res.* **27**, 2171–2179 (1991).

63. Leng, M. J. & Anderson, N. J. Isotopic variation in modern lake waters from western Greenland. *The Holocene* **13**, 605–611 (2003).

64. Gibson, J., Prepas, E. & McEachern, P. Quantitative comparison of lake throughflow, residency, and catchment runoff using stable isotopes: modelling and results from a regional survey of Boreal lakes. *J. Hydrol.* **262**, 128–144 (2002).

65. Cluett, A. A. & Thomas, E. K. Resolving combined influences of inflow and evaporation on western Greenland lake water isotopes to inform paleoclimate inferences. *J. Paleolimnol.* **63**, 251–268 (2020).

66. Rach, O., Kahmen, A., Brauer, A. & Sachse, D. A dual-biomarker approach for quantification of changes in relative humidity from sedimentary lipid D∕H ratios. *Clim. Past* **13**, 741 (2017).

67. Neukom, R. et al. Inter-hemispheric temperature variability over the past millennium. *Nat. Clim. Change* **4**, 362–367 (2014).

68. Von Gunten, L., D'andrea, W. J., Bradley, R. S. & Huang Y. Proxy-to-proxy calibration: Increasing the temporal resolution of quantitative climate reconstructions. *Sci. Rep.* **2**, 609 (2012).

69. Van der Putten, N., Mauquoy, D., Verbruggen, C. & Björck, S. Subantarctic peatlands and their potential as palaeoenvironmental and palaeoclimatic archives. *Quat. Int.* **268**, 65–76 (2012).

70. Shuman, B. Controls on loss-on-ignition variation in cores from two shallow lakes in the northeastern United States. *J. Paleolimnol.* **30**, 371–385 (2003).

71. Whitney, B. S. & Mayle, F. E. Pediastrum species as potential indicators of lake-level change in tropical South America. *J. Paleolimnol.* **47**, 601–615 (2012).

72. Markgraf, V. et al. Holocene palaeoclimates of southern Patagonia: limnological and environmental history of Lago Cardiel, Argentina. *The Holocene* **13**, 581–591 (2003).

73. Blokker, P. et al. Chemical structure of algaenans from the fresh water algae Tetraedron minimum, Scenedesmus communis and Pediastrum boryanum. *Org. Geochem.* **29**, 1453–1468 (1998).

74. Van der Putten, N., Stieperaere, H., Verbruggen, C. & Ochyra, R. Holocene palaeoecology and climate history of South Georgia (sub-Antarctica) based on a macrofossil record of bryophytes and seeds. *The Holocene* **14**, 382–392 (2004).

75. Van Der Putten, N. et al. Peat bank growth, Holocene palaeoecology and climate history of South Georgia (sub-Antarctica), based on a botanical macrofossil record. *Quat. Sci. Rev.* **28**, 65–79 (2009).

76. Mayr, C. et al. Precipitation origin and evaporation of lakes in semi-arid Patagonia (Argentina) inferred from stable isotopes (δ18O, δ2H). *J. Hydrol.* **334**, 53–63 (2007).

77. Kappen, L. & Straka, H. Pollen and spores transport into the Antarctic. *Polar Biol.* **8**, 173–180 (1988).

78. Scott, L. & van Zinderen Barker Sr, E. Exotic pollen and long-distance wind dispersal at a sub-Antarctic Island. *Grana* **24**, 45–54 (1985).

79. Garreaud, R., Lopez, P., Minvielle, M. & Rojas, M. Large-scale control on the Patagonian climate. *J. Climate* **26**, 215–230 (2013).

80. Lamy, F. et al. Holocene changes in the position and intensity of the southern westerly wind belt. *Nat. Geosci.* **3**, 695–699 (2010).

81. Etourneau, J. et al. Holocene climate variations in the western Antarctic Peninsula: evidence for sea ice extent predominantly controlled by changes in insolation and ENSO variability. *Clim. Past* **9**, 1431–1446 (2013).

82. Groff, D. V. et al. Seabird establishment during regional cooling drove a terrestrial ecosystem shift 5000 years ago. *Sci. Adv.* **6**, eabb2788 (2020).

83. Barbraud, C. et al. Effects of climate change and fisheries bycatch on Southern Ocean seabirds: a review. *Mar. Ecol. Prog. Ser.* **454**, 285–307 (2012).

84. Sallée, J.-B., Speer, K. & Rintoul, S. Zonally asymmetric response of the Southern Ocean mixed-layer depth to the Southern Annular Mode. *Nat. Geosci.* **3**, 273–279 (2010).

85. Moreno, P. I. et al. Southern Annular Mode-like changes in southwestern Patagonia at centennial timescales over the last three millennia. *Nat. Commun.* **5**, 4375 (2014).

86. Purich, A., Cai, W., England, M. H. & Cowan, T. Evidence for link between modelled trends in Antarctic sea ice and underestimated westerly wind changes. *Nat. Commun.* **7**, 10409 (2016).

87. Gillett, N. & Fyfe, J. Annular mode changes in the CMIP5 simulations. *Geophys. Res. Lett.* **40**, 1189–1193 (2013).

88. Yuan, X., Kaplan, M. R. & Cane, M. A. The interconnected global climate system—A review of tropical–polar teleconnections. *J. Climate* **31**, 5765–5792 (2018).

89. Yan, H. et al. A record of the Southern Oscillation Index for the past 2,000 years from precipitation proxies. *Nat. Geosci.* **4**, 611–614 (2011).

90. Dätwyler, C., Abram, N. J., Grosjean, M., Wahl, E. R. & Neukom, R. El Niño–Southern Oscillation variability, teleconnection changes and responses to large volcanic eruptions since AD 1000. *Int. J. Climatol.* **39**, 2711–2724 (2019).

91. Fogt, R. L. & Bromwich, D. H. Decadal variability of the ENSO teleconnection to the high-latitude South Pacific governed by coupling with the Southern Annular Mode. *J. Climate* **19**, 979–997 (2006).

92. Cai, W., Sullivan, A. & Cowan, T. Interactions of ENSO, the IOD, and the SAM in CMIP3 models. *J. Climate* **24**, 1688–1704 (2011).
93. Makou, M. C., Eglinton, T. I., Oppo, D. W. & Hughen, K. A. Postglacial changes in El Niño and la Niña behavior. *Geology* **38**, 43–46 (2010).
94. Moy, C. M., Seltzer, G. O., Rodbell, D. T. & Anderson, D. M. Variability of El Niño/Southern Oscillation activity at millennial timescales during the Holocene epoch. *Nature* **420**, 162–165 (2002).
95. Chiang, J. C. & Friedman, A. R. Extratropical cooling, interhemispheric thermal gradients, and tropical climate change. *Ann. Rev. Earth. Planet. Sci.* **40**, 383–412 (2012).
96. Deininger, M. et al. Inter-hemispheric synchroneity of Holocene precipitation anomalies controlled by Earth's latitudinal insolation gradients. *Nat. Commun.* **11**, 1–9 (2020).
97. Broccoli, A. J., Dahl, K. A. & Stouffer, R. J. Response of the ITCZ to Northern Hemisphere cooling. *Geophys. Res. Lett.* **33**, (2006).
98. Thompson, D. W., Wallace, J. M., Kennedy, J. J. & Jones, P. D. An abrupt drop in Northern Hemisphere sea surface temperature around 1970. *Nature* **467**, 444–447 (2010).
99. Kang, S. M., Frierson, D. M. & Held, I. M. The tropical response to extratropical thermal forcing in an idealized GCM: The importance of radiative feedbacks and convective parameterization. *J. Atmos. Sci.* **66**, 2812–2827 (2009).
100. Schneider, T., Bischoff, T. & Haug, G. H. Migrations and dynamics of the intertropical convergence zone. *Nature* **513**, 45–53 (2014).
101. Dai, A. & Wigley, T. Global patterns of ENSO-induced precipitation. *Geophys. Res. Lett.* **27**, 1283–1286 (2000).
102. Ceppi, P., Hwang, Y. T., Liu, X., Frierson, D. M. & Hartmann, D. L. The relationship between the ITCZ and the Southern Hemispheric eddy-driven jet. *J. Geophys. Res. Atmos.* **118**, 5136–5146 (2013).
103. Byrne, M. P., Pendergrass, A. G., Rapp, A. D. & Wodzicki, K. R. Response of the intertropical convergence zone to climate change: Location, width, and strength. *Curr. Clim. Change Rep.* **4**, 355–370 (2018).
104. Baker, P. A. et al. The history of South American tropical precipitation for the past 25,000 years. *Science* **291**, 640–643 (2001).
105. Mayle, F. E., Burbridge, R. & Killeen, T. J. Millennial-scale dynamics of southern Amazonian rain forests. *Science* **290**, 2291–2294 (2000).
106. Haug, G. H., Hughen, K. A., Sigman, D. M., Peterson, L. C. & Röhl, U. Southward migration of the intertropical convergence zone through the Holocene. *Science* **293**, 1304–1308 (2001).
107. Kaufman, D. S. et al. Recent warming reverses long-term Arctic cooling. *Science* **325**, 1236–1239 (2009).
108. Marsicek, J., Shuman, B. N., Bartlein, P. J., Shafer, S. L. & Brewer, S. Reconciling divergent trends and millennial variations in Holocene temperatures. *Nature* **554**, 92 (2018).
109. Bader, J. et al. Global temperature modes shed light on the Holocene temperature conundrum. *Nat. Commun.* **11**, 1–8 (2020).
110. Kaufman, D. et al. Holocene global mean surface temperature, a multi-method reconstruction approach. *Sci. Data* **7**, 1–13 (2020).
111. Balascio, N. L., D'Andrea, W. J., Gjerde, M., & Bakke, J. Hydroclimate variability of High Arctic Svalbard during the Holocene inferred from hydrogen isotopes of leaf waxes. *Quat. Sci. Rev.* **183**, 177–187 (2016).
112. Poynter, J. & Eglinton, G. 14. Molecular composition of three sediments from hole 717c: the Bengal fan. In *Proceedings of the Ocean Drilling Program: Scientific Results* Vol. 116 (1990).
113. Polissar, P. J. & D'Andrea, W. J. Uncertainty in paleohydrologic reconstructions from molecular δD values. *Geochim. Cosmochim. Acta* **129**, 146–156 (2014).
114. Rach, O., Brauer, A., Wilkes, H. & Sachse, D. Delayed hydrological response to Greenland cooling at the onset of the Younger Dryas in western Europe. *Nat. Geosci.* **7**, 109–112 (2014).
115. Dean, Jr W. E. Determination of carbonate and organic matter in calcareous sediments and sedimentary rocks by loss on ignition: comparison with other methods. *J. Sediment. Res.* **44**, 242–248 (1974).
116. Faegri, K., Kaland, P. E. & Krzywinski, K. *Textbook of Pollen Analysis* (John Wiley & Sons Ltd., 1989).
117. Barrow, C. Palynological studies in South Georgia: I. Pollen and spore morphology of the vascular species. *Br. Antarct. Sur. Bull.* **43**, 63–75 (1976).
118. Field, A. *Discovering Statistics Using IBM SPSS Statistics* (Sage, 2013).
119. Killick, R. & Eckley, I. changepoint: an R package for changepoint analysis. *J. Stat. Software* **58**, 1–19 (2014).
120. Braak, C. T. *CANOCO-a FORTRAN Programme for Canonical Community Ordination by [partial][detrended][canonical] Correspondence Analysis, Principal Components Analysis and Redundancy Analysis (version 2.1).* Agricultural Mathematics Group (1988).
121. Šmilauer, P. & Lepš, J. *Multivariate Analysis of Ecological Data Using CANOCO 5* (Cambridge Univ. Press, 2014).
122. Hersbach, H. et al. The ERA5 global reanalysis. *Quart. J. R. Meteorol. Soc.* **146**, 1999–2049 (2020).
123. Draxler, R. & Rolph, G. HYSPLIT (HYbrid Single-Particle Lagrangian Integrated Trajectory) model access via NOAA ARL READY website (http://ready.arl.noaa.gov/HYSPLIT.php). NOAA Air Resources Laboratory. **25**, (2010).
124. Orsi, A. H., Whitworth, T. & Nowlin, W. D. On the meridional extent and fronts of the Antarctic circumpolar current. *Deep Sea Res. I: Oceanogr. Res. Pap.* **42**, 641–673 (1995).

Author contributions

W.G.M.v.d.B. and W.J.D.A. designed the study. W.G.M.v.d.B. and L.T.O. wrote the paper. W.J.D.A., L.T.O., M.Z., and W.G.M.v.d.B. performed the analyses. J.B. and A.E.B. led fieldwork. All authors contributed to the main text during multiple rounds of comments.

Competing interests

The authors declare no competing interests

Additional information

Supplementary information The online version contains supplementary material available at https://doi.org/10.1038/s43247-022-00512-8.

Correspondence and requests for materials should be addressed to Willem G. M. van der Bilt.

Peer review information *Communications Earth & Environment* thanks S. Ladd, Nathalie van der Putten and the other, anonymous, reviewer(s) for their contribution to the peer review of this work. Primary Handling Editors: Olga Churakova, Joe Aslin, Clare Davis. Peer reviewer reports are available.

Reprints and permission information is available at http://www.nature.com/reprints

Publisher's note Springer Nature remains neutral with regard to jurisdictional claims in published maps and institutional affiliations.